

Resolving the molecular environment of Super Star Clusters in Henize 2–10

G. Santangelo^{1,2,3}, L. Testi^{1,4}, L. Gregorini^{2,3}, S. Leurini¹, L. Vanzani⁵, C.M. Walmsley⁴, and D.J. Wilner⁶

¹ European Southern Observatory, Karl Schwarzschild str.2, D-85748 Garching bei Muenchen, Germany
e-mail: gsantang@eso.org, ltesti@eso.org

² INAF - Istituto di Radioastronomia, via Gobetti 101, 40129 Bologna, Italy

³ Dipartimento di Astronomia, Università di Bologna, via Ranzani 1, 40127 Bologna, Italy

⁴ INAF - Osservatorio Astrofisico di Arcetri, Largo E. Fermi 5, I-50125 Firenze, Italy

⁵ Pontificia Universidad Católica de Chile, Departamento de Ingeniería Eléctrica, Av. Vicuña Mackenna 4860, Santiago, Chile

⁶ Harvard-Smithsonian Center for Astrophysics, 60 Garden Street, Cambridge, MA 02138, USA

...

ABSTRACT

Context. The rate of star formation both in the Galaxy and in external galaxies should be related to the physical properties of the molecular clouds from which stars form. This is expected for the starbursts found both in irregular galaxies and in some mergers. The dwarf galaxy Henize 2-10 is particularly interesting in this context as it shows a number of newly formed Super Star Clusters (SSCs) associated with a very rich molecular environment.

Aims. We present a high angular resolution study of the molecular gas associated with the SSCs with the aim of deriving the physical properties of the parent molecular clouds. The final goal is to test the expectation that the formation of SSCs requires exceptionally dense and massive clouds.

Methods. We have used the Submillimeter Array with an angular resolution of $1''.9 \times 1''.3$ to map the $J=2-1$ transition of CO in Henize 2-10. Supplementary measurements of HCN($J=1-0$), $^{13}\text{CO}(J=2-1)$ and millimeter continuum were obtained with the APEX, IRAM 30m and SEST single dish telescopes.

Results. Our single dish observations confirm the association of the newly formed SSCs in Henize 2-10 with dense molecular gas. Our interferometric observations resolve the CO(2-1) emission in several giant molecular clouds. Overall the molecular gas accounts for approximately half of the mass in the central regions of Henize 2-10. Although we find indications that the molecular clouds associated with the formation of SSCs in Henize 2-10 are massive and dense, the tracer we used (CO) and the linear resolution of our observations (60×80 pc) are still not adequate to test the expectation that exceptionally dense and massive cores are required for SSCs formation.

Key words. Galaxies: dwarf – Galaxies: individual: Henize 2-10 – Galaxies: starburst

1. Introduction

Galactic and extragalactic star formation mostly occurs in “bursts” or clusters and the majority of stars is thought to form in large clusters. However, cluster masses and densities vary greatly even within the Milky Way (see Lada & Lada 2003) where the well studied Orion nebular cluster (ONC) has been estimated to have a mass of order $1800 M_{\odot}$ (Hillenbrand & Hartmann 1998) while the most massive galactic clusters (e.g. Brandner et al. 2008; Dowell et al. 2008) have masses of a few times $10^4 M_{\odot}$. These are dwarfed however by young extragalactic clusters and in particular by the starbursts or super star clusters (SSCs) seen in merging systems (e.g. Whitmore 2002) and in some irregular galaxies (e.g. Elmegreen 2002; Johnson & Koblunick 2003) where masses can reach $10^6 M_{\odot}$. It has been speculated that in this case one may be observing young globular clusters.

One presumes that the diversity between local and distant star formation reflects variation within the molecular clouds from which these clusters form and, in particular, variations in the gas pressure. Indeed, even locally, one observes large differences in the characteristics of nearby clouds with moderate pressures and densities in Taurus cores, which mostly form isolated stars, and higher pressures in the molecular gas in the

Orion cloud neighbouring the ONC. Moreover, both gas pressures and star formation rates are higher in the inner regions of the Milky Way, where most of the young massive star clusters are located, and in external galaxies (e.g. Kennicutt 1998). A summary of the characteristics of both clouds and clusters is given by Tan (2008).

Of particular interest are the youngest extragalactic embedded super star clusters or SSCs which have been identified by the free-free radio emission from their associated HII regions (e.g. Koblunick & Johnson 1999; Tarchi et al. 2000; Johnson & Koblunick 2003). These are similar in many ways to local ultra-compact HII regions but larger and are typically powered by the equivalent of several thousand O stars (e.g. Koblunick & Johnson 1999). It is estimated that their stellar masses exceed $\sim 10^5 M_{\odot}$, their radii are of order of a few parsecs, their electron densities are of order of 10^4 cm^{-3} and their ages are below 1 Myr (Koblunick & Johnson 1999; Vacca et al. 2002; Johnson & Koblunick 2003). Thus their mass is of the same order as galactic GMCs but their dimensions are smaller by an order of magnitude and, correspondingly their densities and pressures are much larger. For an assumed star forming efficiency of around 10%, we might expect to see molecular forerunners of the SSCs with masses of $10^6 M_{\odot}$ and sizes of a few parsecs. One might

hope to detect such precluster “cores” either in molecular line emission or in continuum dust emission.

The dwarf irregular galaxy Henize 2-10 at a distance of 9 Mpc ($H_0=75 \text{ km s}^{-1} \text{ Mpc}^{-1}$, Vacca & Conti 1992; Kobulnicky & Johnson 1999) is a good example of this phenomenon. It contains several times $10^8 M_\odot$ of molecular gas as well as multiple HII regions and young clusters observed at radio, optical, and infrared wavelengths (Kobulnicky & Johnson 1999; Johnson et al. 2000; Vacca et al. 2002; Cabanac et al. 2005). The nebulosity seen in HST images does not coincide well with the radio knots suggesting large amounts of obscuration. It is clear therefore that higher angular resolution observations of the molecular emission are warranted in order to understand the characteristics of the clouds from which the SSCs form. Ultimately of course, one would like to image molecular line emission with a resolution comparable both to the dimensions of the SSCs and the optical images (0.1 arcsec resolution). This is currently not possible but as a first step in this direction, we present here results obtained with the Submillimeter array (SMA) in the CO $J=2-1$ transition (and in the mm continuum) with a resolution of roughly $1''.8$ (80 parsec at the distance of Henize 2-10). This allows us to see the distribution of structures comparable to galactic GMCs and to compare with images at other wavelengths. It also allows us an improved view of the molecular cloud dynamics than available in earlier work (Kobulnicky et al. 1995). Finally, we have obtained supplementary measurements of the millimeter continuum and the HCN($J=1-0$) and $^{13}\text{CO}(J=2-1)$ lines with the SEST, IRAM 30m and APEX single dish telescopes.

This paper is structured as follows. In section 2, we present our observations. In section 3, we present our results and compare with previous CO observations of Henize 2-10. In section 4, we describe our analysis and derive the physical parameters of the detected clouds. In section 5, we discuss the results and finally, in section 6, we present our summary and conclusions.

2. Observations and Data Reduction

2.1. Single-dish observations

2.1.1. IRAM-30m Telescope

Henize 2-10 was observed in the $^{13}\text{CO}(J=2-1)$ (220.399 GHz) and HCN($J=1-0$) (88.63 GHz) lines on December 2007 with the 30m Institut de Radioastronomie Millimétrique (IRAM¹) telescope on Pico Veleta. A single position (08^h36^m15^s.20, -26°24'34".0 [J2000]) was observed. The spectra have a typical beam size of $\sim 11''$ in the $^{13}\text{CO}(J=2-1)$ line and $\sim 28''$ in the HCN($J=1-0$) line. Calibration, pointing and focus checks were performed regularly.

The data processing was done with the CLASS² softwares. The data were converted into flux density units, using $S/T_{\text{mb}} = 4.95 \text{ Jy/K}$ (Rohlfs & Wilson 1996). The $^{13}\text{CO}(J=2-1)$ and HCN($J=1-0$) spectra were smoothed to a velocity resolution of 5 km s^{-1} and 10 km s^{-1} , respectively, and the final rms noise was 40 mJy and 5 mJy per channel, respectively.

¹ This publication is partially based on observations carried out with the IRAM 30m telescope. IRAM is supported by INSU/CNRS (France), MPG (Germany) and IGN (Spain).

² See <http://www.iram.fr/IRAMFR/GILDAS> for more information about the GILDAS softwares.

2.1.2. APEX Telescope

We observed Henize 2-10 in the $^{13}\text{CO}(J=2-1)$ (220.399 GHz) with the Atacama Pathfinder Experiment telescope (APEX³, Güsten et al. 2006) on August 28th and 31st 2008 and on December 17th 2008, in the same position used for the IRAM-30m observations. The typical FWHM beam size for the 12m antenna at the $^{13}\text{CO}(J=2-1)$ frequency is $28''$. The line was measured in upper sideband (USB) using the APEX-1 facility receiver in combination with the Fast Fourier Transform Spectrometer.

The data were reduced using the CLASS software. A first order polynomial was fitted to the line-free channels and subtracted off the baseline. We have converted our line intensities into a flux density scale, assuming the aperture efficiency observationally determined by Güsten et al. (2006): 1 K of antenna temperature corresponds to 39 Jy. To increase the signal to noise ratio, the spectrum was smoothed to a velocity resolution of 10.7 km s^{-1} . The noise level in our final spectrum is of the order of 70 mJy per velocity channel.

2.1.3. SEST Telescope

Henize 2-10 was mapped in the 1.2 mm continuum with the bolometer array SIMBA at the SEST on the nights 7-8 and 8-9 June 2002. The beam size of the SEST at this wavelength is $21''$. Background subtraction was obtained by fast scanning ($80''/\text{sec}$) of the source through the array field of view in AZ and ALT, the map size was $480'' \times 240''$. The atmosphere opacity was $\tau \sim 0.1$ during the observations. We reduced the data with the MOPSI (Zylka 1998) package. The total integration time was 4 hours and 50 minutes. The flux calibration was obtained by comparison with planet Uranus. We detected an un-resolved source whose flux is $52 \pm 5 \text{ mJy}$.

2.2. Interferometric SMA observations

Submillimeter interferometric observations of Henize 2-10 in the CO($J=2-1$) (230.538 GHz) line were carried out on February and March 2008 with the Submillimeter Array⁴ (Ho et al. 2004). We obtained data with the array in the extended and compact configurations, half track each, and with six antennas and seven antennas respectively. The phase centre of the observations was the same position used for the IRAM-30m observations. The range of baselines of our dataset spans from the shadowing limit to $\sim 220 \text{ m}$. The observations cycled between Henize 2-10 and two gain calibrators (0826-225 and 0730-116), with 15 minutes on the target and 7 minutes on the calibrators. Passband calibration was ensured observing 3C273 and 3C279. 0730-116 was used to set the absolute flux scale. The flux of this calibrator at the time of observations was determined using values from monitoring observations of the SMA standards (moons and planets). The SMA receivers operate in a double-side band mode, with the upper and lower side bands separated by 8 GHz. We tuned

³ This publication is partially based on data acquired with the Atacama Pathfinder Experiment (APEX, ESO project 081.F-9813). APEX is a collaboration between the Max-Planck-Institut für Radioastronomie, the European Southern Observatory, and the Onsala Space Observatory.

⁴ The Submillimeter Array is a joint project between the Smithsonian Astrophysical Observatory and the Academia Sinica Institute of Astronomy and Astrophysics and is funded by the Smithsonian Institution and the Academia Sinica.

to observe the CO(2-1) in the upper sideband and the $^{13}\text{CO}(2-1)$ and $\text{C}^{18}\text{O}(2-1)$ in the lower sideband.

The initial flagging and calibration of the raw visibility data were done using the IDL-based MIR package⁵. The MIRIAD package was used for imaging and deconvolution of the calibrated visibilities and for the data analysis. The continuum was constructed from the line free channels in the visibility domain. Continuum and line maps from the combined datasets were made with natural weighting, providing a final synthesized beam FWHM of $1''.9 \times 1''.3$ (at a position angle of 5 deg) for the line map, which corresponds to a physical size of 80×60 pc for Henize 2-10, and of $1''.9 \times 1''.4$ (at a position angle of 6 deg) for the continuum map. The rms noise is 19 mJy beam^{-1} per 5 km s^{-1} channel in the CO($J=2-1$) line data and 1 mJy beam^{-1} in the continuum.

3. Results

3.1. Millimeter Continuum

No millimeter continuum detection was obtained at the high angular resolution of the SMA. We obtain no clear detection above a 5σ upper limit of 5 mJy/beam , which converts into a total gas+dust mass between $5 \cdot 10^6 M_{\odot}$ and $1.6 \cdot 10^7 M_{\odot}$, assuming a range of temperatures between 20 K and 50 K and a dust opacity of $0.005 \text{ cm}^2 \text{ g}^{-1}$ (see discussion in section 4.3).

Our SIMBA single dish 1.2 mm flux is consistent with the MAMBO 1.3 mm flux of $\sim (56 \pm 14) \text{ mJy}$ reported by Galliano et al. (2005), while, integrating the SMA continuum map over the 30m beam, we recover 17 mJy with the interferometer, which is the 30% of the single dish flux. The most likely explanation, given also the extent ($\sim 15''$) of the 450 and $850 \mu\text{m}$ emission detected by Galliano et al. (2005), is that our interferometric observations filter out the most extended emission. To estimate this effect we used the approach outlined by Wilner & Welch (1994). Given a minimum baseline length, their formalism allows us to estimate the fraction of flux seen by the interferometer for a Gaussian source with a given FWHM. For our observations, the minimum projected baseline of $7 \text{ k}\lambda$, where λ is the wavelength of our observations, allows us to recover 100% of the total flux for sources comparable to the beamsize, but only $\sim 40\%$ of the total flux density for a source of FWHM $15''$ (650 pc at a distance of 9 Mpc).

3.2. Molecular Gas Morphology

3.2.1. Single dish observations

In Fig. 1, we show the observed IRAM-30m spectra of the $^{13}\text{CO}(J=2-1)$ and HCN($J=1-0$) transitions. Both lines are detected and they are approximately 100 km s^{-1} wide, consistent with previous observations of CO and isotopologues by Kobulnicky et al. (1995).

The line parameters have been estimated fitting a Gaussian profile to each spectrum. Table 1 summarizes the beam size at the observed frequencies, the peak and integrated flux densities and the line width of the observed emission lines.

The HCN(1-0) total intensity that we derive from our spectrum ($\leq 2 \text{ Jy km s}^{-1}$) is significantly lower than the value found by Imanishi et al. (2007) in their NMA integrated map ($\sim 6 \text{ Jy km s}^{-1}$). This is surprising as the single dish telescope

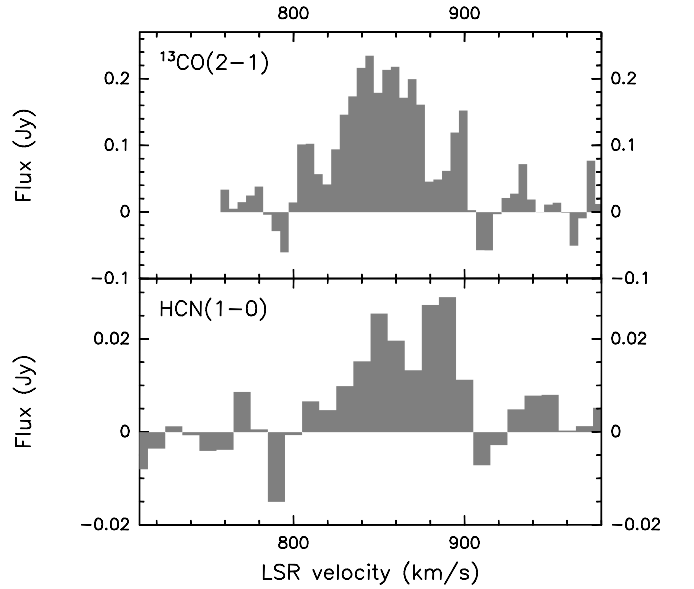


Fig. 1. $^{13}\text{CO}(J=2-1)$ (top) and HCN($J=1-0$) (bottom) IRAM-30m spectra.

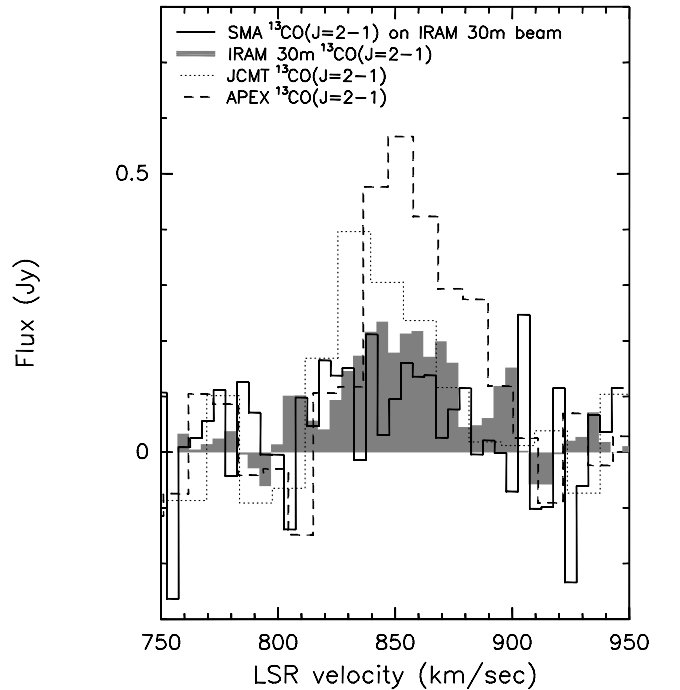


Fig. 2. Comparison between the $^{13}\text{CO}(J=2-1)$ spectra from IRAM-30m (grey shaded), SMA (solid line, integrated over the IRAM-30m beam area), JCMT (dotted line; Baas et al. 1994) and APEX (dashed line).

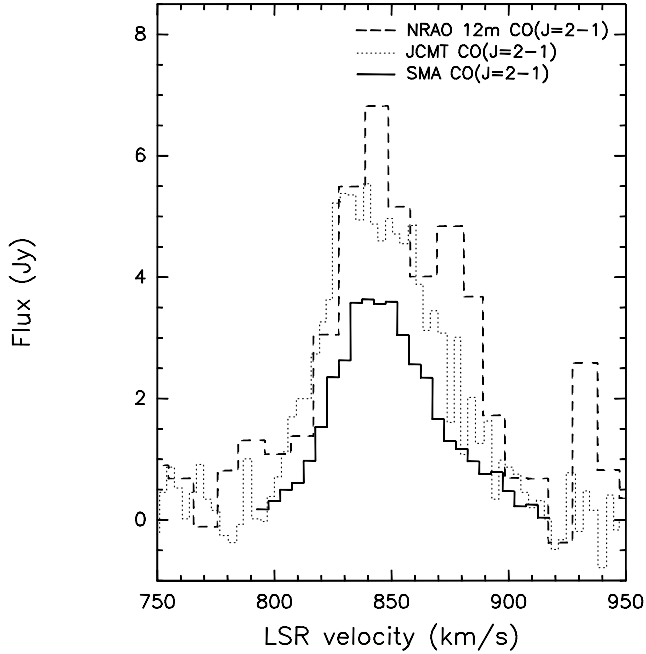
should have detected the same or more emission than the interferometer. Both the IRAM-30m and the NMA detections do not have a very high signal to noise ratio and higher sensitivity observations will be needed in the future to confirm the flux of this source. We cannot exclude the possibility of a problem with the calibration of the IRAM spectrum.

In Fig. 2 we show the observed APEX $^{13}\text{CO}(J=2-1)$ spectrum (dashed line). The parameters of the emission line from a Gaussian fit to the spectrum are presented in Table 1. In the same figure we show also the IRAM-30m spectrum (grey shaded) and

⁵ <http://sma-www.cfa.harvard.edu/miriadWWW/manuals/SMAguide/smauserhtml/>

Table 1. IRAM-30m and APEX $^{13}\text{CO}(J=2-1)$ and $\text{HCN}(J=1-0)$ emission lines parameters.

Line	Beam Size [arcsec]	Flux _{peak} [Jy]	FWHM [km s ⁻¹]	V _{LSR} [km s ⁻¹]	Integrated Flux [Jy km s ⁻¹]
(1)	(2)	(3)	(4)	(5)	(6)
IRAM-30m					
$^{13}\text{CO}(J=2-1)$	11	0.21	56	850	13±1
$\text{HCN}(J=1-0)$	28	0.025	64	860	2.0±0.5
APEX					
$^{13}\text{CO}(J=2-1)$	28	0.5	42	855	22±2

**Fig. 3.** Comparison between the NRAO-12m $\text{CO}(J=2-1)$ spectrum (dashed line) from Kobulnicky et al. (1995), our SMA $\text{CO}(J=2-1)$ spectrum (solid line), integrated over the whole region of the emission, and the JCMT $\text{CO}(J=2-1)$ spectrum (dotted line) from Baas et al. (1994).

the JCMT spectrum from Baas et al. (1994, dotted line). Figure 2 shows that the IRAM-30m $^{13}\text{CO}(J=2-1)$ spectrum is fainter than both the JCMT and the APEX spectra. This could be due to either a problem in the calibration or pointing of the IRAM-30m data, because of the large airmass of this southern object, or to the fact that the $^{13}\text{CO}(J=2-1)$ emission is more extended than the IRAM-30m beam (11'' at this frequency). Therefore part of the emission which is seen by APEX and JCMT, with beam sizes of 28'' and 21'' respectively, is outside the IRAM beam. This explanation is consistent with the SCUBA continuum maps of Galliano et al. (2005), the non-detection of the $^{13}\text{CO}(J=2-1)$ emission with the SMA (see below) and the detection of an extended component in the $\text{CO}(J=3-2)$ emission by Vanzi et al. (2009).

3.2.2. Comparison between single dish and interferometer

Figure 3 shows the NRAO $\text{CO}(J=2-1)$ spectrum (dashed line) from Kobulnicky et al. (1995) overlaid on our SMA integrated spectrum (solid line) and the JCMT $\text{CO}(J=2-1)$ spectrum from Baas et al. (1994, dotted line). The comparison shows that we recover 44% of the single dish flux density, while the remain-

ing part, which most probably comes from extended emission, is filtered out by the interferometer.

Kobulnicky et al. (1995) found an elongated cloud of molecular gas with a tail towards the south-east. This tail, revealed in the OVRO $\text{CO}(J=1-0)$ map in a velocity interval between 805 and 835 km s⁻¹, is not seen in our SMA $\text{CO}(J=2-1)$ data (with the exception of two 3 σ level peaks), most likely because the higher resolution SMA observations filter out this extended emission.

As mentioned before, the correlator frequency coverage and configuration were such that also $^{13}\text{CO}(J=2-1)$ and $\text{C}^{18}\text{O}(J=2-1)$ transitions were observed. From our IRAM-30m observations of $^{13}\text{CO}(J=2-1)$ we expect a peak flux density of about 0.2 Jy on a beam size of around 11''. The spectrum of our SMA $^{13}\text{CO}(J=2-1)$ observations integrated over the IRAM beam is shown in Fig. 2, overlaid on the IRAM-30m $^{13}\text{CO}(J=2-1)$ spectrum, the JCMT $^{13}\text{CO}(J=2-1)$ spectrum from Baas et al. (1994) and the APEX $^{13}\text{CO}(J=2-1)$ spectrum. The rms of the SMA spectrum (roughly 0.1 Jy) is about half of the peak flux expected from the single dish IRAM observations and does not permit a credible detection. The $\text{C}^{18}\text{O}(J=2-1)$ emission, as one might expect, was detected neither in the APEX spectrum nor by the SMA.

The non-detection of the $^{13}\text{CO}(2-1)$ line and the large fraction of the $\text{CO}(2-1)$ flux that is not recovered by our SMA observations are consistent with the presence of extended molecular emission to which the SMA is not sensitive, as discussed in the previous paragraph, and with the fact that the SMA is only recovering a fraction of the millimeter continuum emission.

3.2.3. Morphology of the molecular gas emission

Our SMA spectral line data resolve the OVRO $\text{CO}(J=1-0)$ emission from Kobulnicky et al. (1995) into several compact sources. The velocity structure of the $\text{CO}(J=2-1)$ emission is given in Fig. 4, which shows the channel map of the $\text{CO}(J=2-1)$ emission. The map reveals the complex velocity structure of the CO emission, with most of the emission centred on an LSR velocity around 850 km s⁻¹. Several velocity components can be distinguished in the emission and some of them are comparable with the beam size. The CO components are well separated in both position and velocity and spread over a velocity interval of about 100 km s⁻¹, as already revealed from the single dish observations of $^{13}\text{CO}(J=2-1)$ and $\text{HCN}(J=1-0)$ (see Fig. 1 and Fig. 2).

Figure 5 shows the SMA $\text{CO}(J=2-1)$ velocity-integrated intensity map in solid contours overlaid on the VLA 3.6 cm continuum (Johnson & Kobulnicky 2003). Part of the centimeter continuum emission, associated with the super star clusters, is coincident with the most compact molecular gas sources in the $\text{CO}(J=2-1)$ emission line. In particular, the centimeter sources 1, 2 and 5 (see Johnson & Kobulnicky 2003) correspond respec-

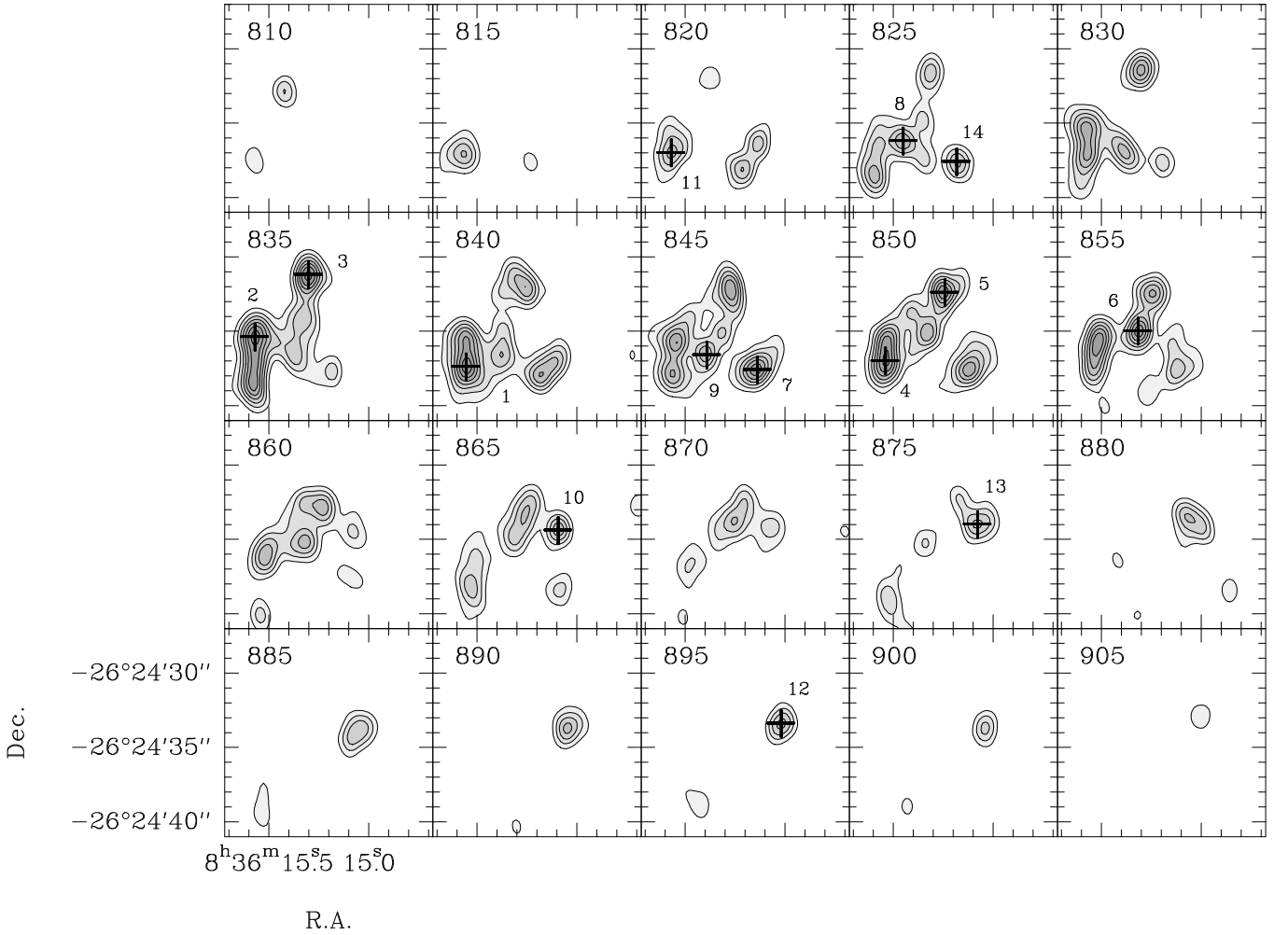


Fig. 4. Channel map of the CO($J=2-1$) line. The contour levels are from 5σ ($\sigma=19$ mJy/beam) in steps of 3σ . The black numbered crosses indicate the peak position (in the channel corresponding to the peak velocity) of the emission of the 14 molecular clouds identified by the Clumpfind algorithm (see §4.1 and Table 3).

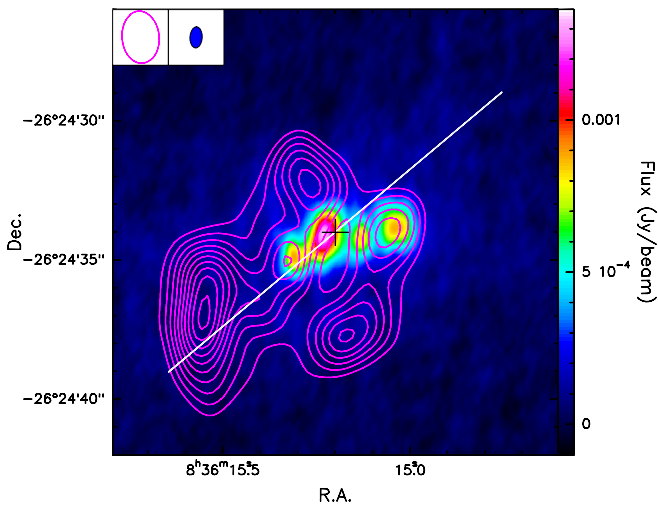


Fig. 5. SMA integrated CO($J=2-1$) map (contours), overlaid on the VLA 3.6 cm continuum image from Johnson & Kobulnicky (2003). The contour levels are from 5σ in steps of 2σ ($\sigma=0.8$ Jy beam $^{-1}$ km s $^{-1}$). The white line and the cross indicate respectively the orientation of the position-velocity cut, shown in Fig. 6 (see §5.1), and the central position of the map.

Table 2. Integrated SMA CO($J=2-1$) and $^{13}\text{CO}(J=2-1)$ lines parameters.

Line	Flux _{peak} [Jy]	FWHM [km s $^{-1}$]	V _{LSR} [km s $^{-1}$]	Integrated Flux [Jy km s $^{-1}$]
(1)	(2)	(3)	(4)	
$^{12}\text{CO}(J=2-1)$	3.5	48	846	178.4 \pm 1.6
$^{13}\text{CO}(J=2-1)$	$\lesssim 0.3$	–	–	$\lesssim 12$

tively to our sources 12, 13 and 6 (see Fig. 4 and Table 3). Some of the CO emission is not associated with the SSCs.

The strongest 3.6 cm source, which does not correspond to any significant amount of molecular emission, is likely in an older evolutionary stage, having already dispersed most of the surrounding molecular material from which it formed.

We performed Gaussian fits to the spectra of the lines observed with SMA, integrated over the whole region of the emission, to estimate the peak and integrated flux density and the line width of the observed emission lines. Table 2 summarizes the fitting parameters. The values of the peak and integrated flux densities of the $^{13}\text{CO}(J=2-1)$ emission line, observed with SMA, are upper limits because the line is not detected. It is thus possible to derive a lower limit to the flux density ratio between

the CO($J=2-1$) and $^{13}\text{CO}(J=2-1)$ emission lines. We estimate a CO($J=2-1$)/ $^{13}\text{CO}(J=2-1)$ ratio $\gtrsim 14.9$.

4. The structure of the CO($J=2-1$) emission

4.1. Identification of the clouds: Clumpfind

We applied the Clumpfind algorithm (Williams et al. 1994) to the SMA CO($J=2-1$) data cube to decompose the emission into discrete structures and identify the individual molecular clouds. Clumpfind works by making a contour map through the data cube to locate the peak flux densities and then steps down the contour levels to determine where the clumps are located. Clumpfind allows the user to adjust the contour spacing and the lower contour level. The advantage of this algorithm is that we make no assumptions about the cloud shape. The specific intensity contour used as emission threshold, which defines the borders (boundaries) of the individual identified clouds, is 0.1 Jy/beam, corresponding to 5σ level. The step level used to disentangle the emission and identify isolated peaks is 60 mJy/beam (3σ). To be sure the algorithm is not introducing artefacts, we decided to limit the analysis to the clouds with peak flux density larger than 15σ . In this way, we identified 14 separate CO clouds.

It is important to realize that the Clumpfind algorithm does not take into account effects of self-absorption, which manifest in a double peak line profile: it would then try to separate the two peaks of a single self-absorbed clump spectrum in two distinct clouds with same spatial position and different velocity. With our data we do not see a clear evidence that this is effecting a significant fraction of the clumps we identify, as most of the clumps are also spatially distinct.

To emphasize the complex substructure of the emission we marked with black crosses in Fig. 4 (the channel map of the emission) the position of the clouds identified by the Clumpfind algorithm, in the channel relative to the peak of each cloud emission. The 14 components are well visible in the plot and are labeled by their respective number.

The parameters for our final cloud decomposition of the data set, given by Clumpfind, are presented in Table 3. The angular sizes have been computed from the 5σ contour levels and deconvolved with a simple Gaussian deconvolution for the beam size, assuming source and beam to be Gaussian. The velocity widths have been deconvolved as well for the velocity resolution. Table 3 gives also the derived masses of the identified clouds (see next section for the details).

4.2. Derivation of Physical Parameters of the Clouds

Several methods can be used to obtain molecular mass estimates. The molecular hydrogen column density, $N(\text{H}_2)$, can be estimated from the CO flux, S_{CO} , using a CO-to- H_2 conversion factor, X_{CO} ($X_{\text{CO}}=N(\text{H}_2)/I_{\text{CO}}$), which is empirically determined from Galactic molecular clouds. It is a matter of debate what is the best choice for X_{CO} . Dwarf galaxies, possibly due to their low metallicities, seem to have a higher standard conversion factor than large metal-rich spirals (Maloney & Black 1988; Verter & Hodge 1995; Wilson 1995; Arimoto et al. 1996). However, Henize 2-10 is a dwarf galaxy with roughly solar metallicity ($12+\log(\text{O}/\text{H})=8.93$; Vacca & Conti 1992). Moreover, Blitz et al. (2007), studying extragalactic Giant Molecular Clouds (GMCs), conclude that there is no clear trend of X_{CO} with metallicity. We thus estimate the molecular mass (M_{mol}) of the clouds using the Galactic value for the CO-to- H_2 conversion factor, $X_{\text{COgal}} =$

$(3 \pm 1) \times 10^{20} \text{ cm}^{-2} (\text{K km s}^{-1})^{-1}$ (Strong et al. 1988; Sanders et al. 1987) which also includes a factor of 1.36 to account for the helium mass contribution. Following Wilson & Scoville (1990) we use:

$$M_{\text{mol}} = 1.61 \times 10^4 \left(\frac{115 \text{ GHz}}{\nu} \right)^2 d_{\text{Mpc}}^2 \frac{S_{\text{CO}}}{R_{21}} M_{\odot} \quad (1)$$

where S_{CO} is the CO($J=2-1$) flux in Jy km s^{-1} , d_{Mpc} is the distance and R_{21} is the CO($J=2-1$)/CO($J=1-0$) line ratio, which we assumed equal to 0.89 (Braine et al. 1993). The latter value is also consistent with the range of ratios derived for this galaxy (Meier et al. 2001; Baas et al. 1994) and for dwarf irregular galaxies (Petitpas & Wilson 1998).

The masses of the individual clouds can also be calculated from the measured sizes and velocity dispersions using the virial theorem. The underlying assumption is that the internal kinetic energy and the gravitational energy are in equilibrium (Solomon et al. 1987). Assuming the source to be spherical and homogeneous and neglecting contributions from magnetic field and surface pressure, the virial cloud mass is given by:

$$M_{\text{VIR}} = 0.509 d(\text{kpc}) \Theta_{\text{S}}(\text{arcsec}) \Delta V_{1/2}^2 (\text{km s}^{-1}) M_{\odot} \quad (2)$$

(MacLaren et al. 1988), where $\Delta V_{1/2}$ is the measured full-width velocity at half-maximum intensity in km s^{-1} and Θ_{S} is the cloud angular diameter in arcsec.

The masses derived for each cloud by means of the two different methods described above are presented in Table 3. The values show that the two different methods give very similar results (within a factor typically of 2). In particular, the virial masses are slightly larger than the masses computed using the conversion factor. The two methods used here to determine the masses of the clouds are in reasonable agreement and no clear evidence for a systematic difference between the two determinations can be claimed at this point. There has been much discussion of how well CO intensity can be converted to total molecular gas mass in external galaxies using Galactic conversion factors. However, in the present study we are resolving individual molecular clouds rather than averaging over the entire distribution of clouds. The fact that the masses derived by the two different methods agree within a factor of 2, in spite of the different assumptions made for the two determinations, suggests that there may not be a significant problem in this case.

We also computed the surface density, $\Sigma=M/(\pi R^2)$, of each identified cloud, using both the virial masses and the masses derived with the conversion factor. The values are given in Table 3 (Col. 11 and 12).

4.3. Continuum emission from the molecular clouds

It may appear surprising that we do not detect 1.3mm continuum emission from the clumps seen in the CO emission or from the compact HII regions seen with the VLA (see Fig. 4 and 5). As far as the HII regions are concerned, we note that extrapolation to 230 GHz of the Johnson & Koblunicky (2003) flux of the strongest centimeter continuum source, assuming optically thin free-free emission, yields expected flux densities of 2 mJy or roughly 2σ at our sensitivity. Thus it is not surprising that our observations do not detect the free-free emission from these source, especially if partially resolved.

Table 3. Physical parameters of the SMA CO($J=2-1$) molecular clouds identified with Clumpfind.

N	Peak Position		V_{peak}	S_{peak}	Radius ^a	$\Delta V_{1/2}$ ^a	$S_{\text{CO}(J=2-1)}$	M_{VIR}	M_{mol}	Σ_{VIR}	Σ_{mol}
(1)	R.A.[J2000]	Decl.[J2000]	[km/s]	[Jy/beam]	[arcsec]	[km/s]	[Jy km/s]	[$\times 10^6 M_{\odot}$]	[$\times 10^6 M_{\odot}$]	[g/cm ²]	[g/cm ²]
1	8:36:15.53	-26:24:37.4	840	0.48	1.3	18	10.7	3.6	3.9	0.08	0.09
2	8:36:15.54	-26:24:35.4	835	0.47	1.2	25	13.4	6.9	4.9	0.16	0.11
3	8:36:15.30	-26:24:31.2	835	0.46	1.2	18	7.9	3.3	2.9	0.09	0.08
4	8:36:15.52	-26:24:37.0	850	0.46	0.8	19	7.5	2.9	2.7	0.14	0.14
5	8:36:15.24	-26:24:32.4	850	0.43	1.2	25	12.7	7.1	4.6	0.17	0.11
6	8:36:15.31	-26:24:35.0	855	0.42	1.0	20	8.3	3.9	3.0	0.13	0.10
7	8:36:15.14	-26:24:37.6	845	0.42	1.2	13	8.1	1.9	3.0	0.05	0.07
8	8:36:15.43	-26:24:36.2	825	0.33	0.8	20	5.0	3.0	1.8	0.16	0.09
9	8:36:15.38	-26:24:36.6	845	0.32	1.2	26	8.1	7.4	3.0	0.19	0.07
10	8:36:15.10	-26:24:34.4	865	0.31	1.1	20	4.1	4.0	1.5	0.12	0.05
11	8:36:15.54	-26:24:37.0	820	0.29	1.0	15	5.0	2.1	1.8	0.08	0.06
12	8:36:15.03	-26:24:33.4	895	0.29	1.0	19	5.2	3.1	1.9	0.11	0.07
13	8:36:15.09	-26:24:34.0	875	0.28	0.9	19	5.0	3.1	1.8	0.12	0.07
14	8:36:15.19	-26:24:37.6	825	0.28	1.2	24	5.3	6.5	1.9	0.16	0.05

NOTES. – Col.(1): Number of the cloud. Col.(2)-(3): Peak position of the emission. Col.(4): Peak velocity of the emission. Col.(5): Peak flux density of the emission. Col.(6): Deconvolved radius (at 5σ contour level) of the cloud. Col.(7): Deconvolved FWHM line width. Col.(8): Integrated flux. Col.(9): Virial mass. Col.(10): Molecular gas mass from SMA CO($J=2-1$). Col.(11): Surface density of the clouds, computed from the virial masses (Col.9). Col.(12): Surface density of the clouds, computed from the molecular gas masses (Col.10).

^a Deconvolved.

To compute the expected millimeter continuum flux from the dust, associated with the CO clumps (with gas mass M_g), we can use the equation:

$$M_g = \frac{S_\nu d^2}{\kappa(\nu) B_\nu(T_d)} \quad (3)$$

(Launhardt & Henning 1997), assuming optically thin thermal dust emission and isothermal conditions. $B_\nu(T_d)$ is the Planck function at the assumed dust temperature T_d , d the distance of the object and $\kappa(\nu)$ is the dust opacity per gram of gas. We adopt opacity equal to $0.005 \text{ cm}^2 \text{ g}^{-1}$ (André et al. 2000). For the derived masses of the individual CO clumps in Table 3, we estimate typical 1.3 mm continuum fluxes of 1-2 mJy (or $1-2 \sigma$), for a range of temperatures T_d between 20 K and 50 K. Therefore, it is not surprising that also from the CO clumps we do not detect 1.3 mm continuum emission.

Incidentally, we note that the continuum emission from dust may be a very good tracer of dense and massive molecular clouds. Indeed, an unresolved clump of mass M_{cl} may be more easily detected in continuum emission than in CO. This is because, for a source smaller than the synthesised beam, one has for the ratio of continuum flux S_d to CO flux S_{CO} that:

$$\frac{S_d}{S_{\text{CO}}} = \frac{\kappa(\nu) M_{\text{cl}}}{\pi \Delta \nu R_{\text{cl}}^2} \quad (4)$$

where R_{cl} is the clump radius and $\Delta \nu$ is the CO line width. The latter in a virialised situation is proportional to $(M_{\text{cl}}/R_{\text{cl}})^{0.5}$ and so one concludes that the ratio of continuum to CO fluxes varies as $R_{\text{cl}}^{-1.5}$ for an unresolved clump. We assume in the above that the CO emission is optically thick and thermalised whereas the dust emission is optically thin. For a cloud of radius 10 pc, the ratio is almost ten times larger than the ratio for structures of the size of the beam ($R_{\text{cl}} \sim 40$ pc). This ratio can thus be significant if one is, for example, observing something similar to the "Massive Molecular Aggregates" postulated by Koblunicky & Johnson (2000), which are expected to have masses of order $10^7 M_{\odot}$ and dimensions of order a few parsecs. Such objects would have millimeter fluxes of a few mJy and are barely out of reach for our observations. Clearly, verifying this speculation

requires higher frequency, sensitivity and angular resolution sub-millimeter observations of the continuum from Henize 2-10.

5. Discussion

5.1. Dynamical properties of the molecular gas

An important aim of our study was to examine the kinematics of the molecular clouds for comparison both with the velocity field of the stars (see e.g. Marquart et al. 2007) and with earlier work on the gas kinematics by Koblunicky et al. (1995). This is useful also for comparison with the molecular gas mass estimates derived in the previous section.

Thus in order to investigate the rotation curve in the inner region of Henize 2-10 near the site of massive star formation and compare it with the results of Koblunicky et al. (1995), we extracted a position-velocity diagram by taking a $4''$ wide slice of our SMA CO($J=2-1$) data cube, passing through the brightest optical starburst region, at the same position angle as Koblunicky et al. (1995) ($\text{PA}=130^\circ$), which they find to be the direction of the steepest velocity gradient. The orientation of the position-velocity cut is shown in Fig.5. The position-velocity diagram, shown in Fig. 6, reveals two structures of which the innermost shows spatial velocity variations of 60 km s^{-1} on a scale of 7 arcseconds. This velocity gradient implies a dynamical mass of $1.6 \cdot 10^7 / (\sin i)^2 M_{\odot}$, within a radius of 150 pc, where i is the inclination of the object with respect to the line of sight ($i=90^\circ$ means an edge-on rotating structure).

Koblunicky et al. (1995) detected in their OVRO CO($J=1-0$) data a dynamically distinct feature, which was denoted by the letter "C". This CO feature, around 875 km s^{-1} (see Fig. 6), is also detected in the SMA CO($J=2-1$) integrated map between 875 and 890 km s^{-1} , at the position $\alpha_{2000} = 8^{\text{h}}36^{\text{m}}15^{\text{s}}.5$ and $\delta_{2000} = -26^\circ24'39''$. Its SMA CO deconvolved size is about $1''.8 \times 2''.3$, which corresponds to a linear size of 80×100 pc. Its total integrated flux density is 4 Jy km s^{-1} , consistent with the measurement by Koblunicky et al. (1995), implying a molecular mass of $1.5 \cdot 10^6 M_{\odot}$, using the same method described in section 4.2 (see Eq. 1). Assuming a deconvolved velocity width of 14.1 km s^{-1} and a radius of $1''$, we estimate for this feature a

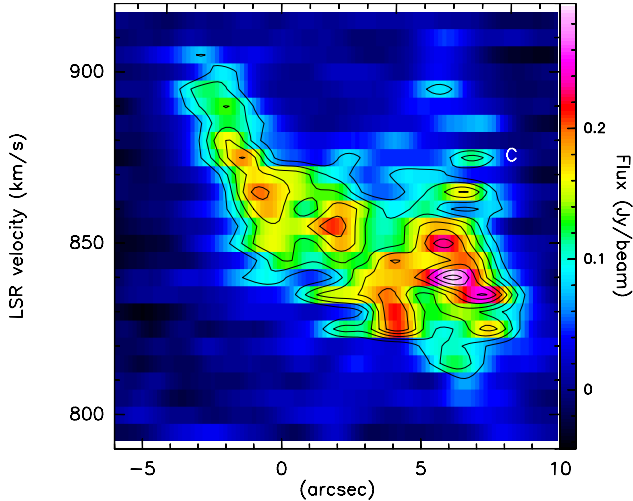


Fig. 6. SMA CO($J=2-1$) position-velocity diagram of Henize 2-10 obtained from a $4''$ wide slice through the data cube, at a position angle of 130° (see Fig. 5), passing through the center of the map: $08^{\text{h}}36^{\text{m}}15^{\text{s}}.20$, $-26^\circ24'34''.0$ (J2000). The horizontal axis represents the positional offset in arcsec with respect to this central position. Contour levels are from 25% to 95% in step of 10% of the peak.

virial mass of $1.8 \cdot 10^6 M_\odot$ (see Eq. 2). This cloud is not listed in Table 3 since its peak flux density is below the detection threshold (15σ , see §4.1) that we have set for the output given by Clumpfind.

It is interesting to compare the derived dynamical mass with the estimated stellar mass within the newly formed super star clusters and the mass of the molecular gas in the region. From our SMA CO($J=2-1$), the mass of the molecular gas within this region is around $10^7 M_\odot$, which means that if the inclination of the molecular rotation axis is 90° (edge-on), the newly formed stars must contain at least 40% of the total mass in the inner 150 pc radius. If the inclination is lower, the total dynamical mass is larger and, given that the total gas mass is determined by our SMA observations, the fraction of the total dynamical mass comprised by the stars will be larger.

Conti & Vacca (1994) present *Hubble Space Telescope* images which show 9 UV-bright knots in the inner 90 pc. They estimate a total mass of newly formed stars of $2.7 \cdot 10^6 M_\odot$. The upper limit to the stellar mass from our SMA observations is $6 \cdot 10^6 M_\odot$ (see above), derived for a region which is about 3 times larger in radius than the one considered by Conti & Vacca (1994). This means that, extrapolating the estimated stellar mass from Conti & Vacca (1994) to the dimensions of our region, one obtains a stellar mass value between $2.7 \cdot 10^6 M_\odot$ and $2.4 \cdot 10^7 M_\odot$, respectively assuming that the stars are concentrated in the inner 90 pc, observed by Conti & Vacca (1994), or uniformly distributed over a region which is 3 times larger in radius. Therefore, the picture presented in Conti & Vacca (1994) is consistent with the estimates which we discuss above.

Another way to estimate the total mass involved in the whole region and how it is distributed between the molecular gas and the stars is to compute the (statistical) velocity dispersion, σ_v , of the clouds identified in the SMA CO($J=2-1$) emission and derive the total mass of the region, assuming virial equilibrium. From Eq. 2, taking the FWHP velocity ($\sqrt{8 \ln(2)} \times \sigma_v$), we derived a total mass of $1.2 \cdot 10^8 M_\odot$. Given that the total gas mass derived from our SMA CO($J=2-1$) data is about $4-6 \cdot 10^7 M_\odot$ (derived

from the molecular and virial masses respectively; see Table 3), we estimate again that the stars should account for $\sim 30-50\%$ of the total mass, without taking into account the contribution from atomic gas, which is difficult to estimate at these angular scales.

Our result is also in agreement with the OVRO CO($J=1-0$) motions measured by Koblunicky et al. (1995). Their study reveals a rotation of the CO gas on large scales, with a velocity gradient which is about half of the gradient derived from our SMA CO data. They find that the low resolution of their observations ($6'.5 \times 5'.5$ beam size) gives only an “average” rotation curve smoothed over the beam and decreases the observed velocity gradient, which is consistent with what we observe. Their estimated dynamical mass is $3.2 \cdot 10^6 / (\sin i)^2 M_\odot$, which implies that the stellar component may contain up to half of the dynamical mass in the inner region, in agreement with our result.

The gas velocity field is also consistent with Marquart et al. (2007). They find spatial velocity variations up to 60 km s^{-1} for the ionized interstellar medium, but no systematic trend in the velocity of the stars and conclude that the stellar kinematics is governed by random motions.

5.2. The physical properties of Clouds associated with SSCs

Some views of cluster formation expect prestellar cores to have the same physical properties as the young stellar clusters they will eventually produce. Indeed, in the Galactic context the Infrared Dark Clouds (IRDCs), considered to be possible high-mass pre-stellar cores and revealed by absorption of the Galactic diffuse infrared background (Perault et al. 1996; Egan et al. 1998), have similar surface densities as clusters associated with young massive stars in our Galaxy (Tan 2008). Therefore, in the extragalactic context, the expectation is to find extremely dense molecular clouds associated with SSCs. However, the limits imposed by the resolution and sensitivity of the existing instruments make difficult the task of testing this scenario and resolving the parent dense cores of the individual SSCs. A 5σ detection of an unresolved clump of $10^6 M_\odot$ requires a sensitivity of $\sim 0.1 \text{ mJy beam}^{-1}$, assuming a temperature of 20 K, still a challenge for the current millimeter interferometric facilities.

The clouds, resolved in the CO($2-1$) emission with the SMA, have masses and surface density values (see Table 3) of the same order of magnitude of the galactic GMCs ($M \sim 10^4 - 10^6 M_\odot$, $\Sigma \sim 0.035 \text{ g cm}^{-2}$; Solomon et al. 1987), but systematically higher. For a virialised cloud, surface density is a measure of pressure and it is comprehensible that the GMCs in Henize 2-10 are at higher pressure than in the Galaxy. Moreover due to our limited angular resolution, our column density estimates may well be considerable underestimates. It seems reasonable therefore that, as in the Milky Way, clusters in Henize 2-10 form from small parsec sized clumps at much higher pressure than the rest of the GMC. Using SMA, we have made a first step towards resolving the molecular clouds associated with the SSCs and towards testing for the presence of very dense and compact molecular clouds, predecessors of the SSCs.

The density traced by the CO($J=2-1$) line is limited (critical density $n_{cr} \sim 2.7 \cdot 10^3 \text{ cm}^{-3}$) and to probe high density molecular gas ($n_{\text{H}_2} > 10^4 \text{ cm}^{-3}$), which is expected to be associated with star (SSCs) forming regions, higher density tracers like HCO⁺ and HCN are needed. Indeed, Henize 2-10 is known to show strong HCO⁺ and HCN emission (Imanishi et al. 2007; our own IRAM 30 m spectrum presented in this paper), which reflect the spatial distribution of the dense molecular gas. The interferometer observations of Imanishi et al. (2007) have a beam size of $5'.5 \times 10'.8$. To compare our SMA CO($J=2-1$) with the NMA

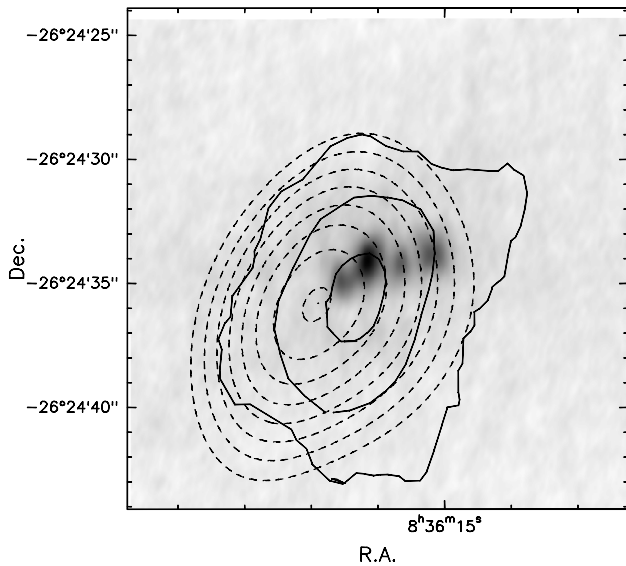


Fig. 7. $\text{HCO}^+(J=1-0)$ integrated map from Imanishi et al. (2007) (beam size of $5''.5 \times 10''.8$, solid contours) and SMA $\text{CO}(J=2-1)$ emission (dashed contours) smoothed to the resolution of the $\text{HCO}^+(J=1-0)$, overlaid on the VLA 3.6 cm continuum in grey scale (Johnson & Koblunicky 2003).

maps of Imanishi et al. (2007), we have smoothed our maps to the same angular resolution. The comparison is shown in Fig. 7. Given that the position calibration uncertainties for the interferometric data are much less than $1''$, the overlay of the $\text{CO}(J=2-1)$ and $\text{HCO}^+(J=1-0)$ emissions seems to reveal a shift between the two molecular emissions, which is almost $2''$. This is surprising on one side because one would expect the $\text{HCO}^+(J=1-0)$, being a tracer of high density gas, to be associated to the peaks of the $\text{CO}(J=2-1)$ molecular emission. On the other hand, the CO distribution is complex in both position and velocity and it is likely that only some of the molecular clouds may be sufficiently dense to show strong $\text{HCO}^+(J=1-0)$ emission and this might produce the shift between the centers of the two integrated emissions. Besides, there might be also an effect due to the different opacity of the two lines. Finally, the $\text{HCO}^+(J=1-0)$ peak from Imanishi et al. (2007) appears to be closer to the SSCs in Henize 2-10 than our SMA $\text{CO}(J=2-1)$ peak. This could mean that the high density gas is mainly close to the SSCs.

Indeed, the sensitivity and resolution of the $\text{HCO}^+(J=1-0)$ observations of Imanishi et al. (2007) are not adequate in space and velocity to resolve the dense gas peaks associated with the SSCs. It is thus necessary to observe high density tracers at higher resolution to resolve the molecular clouds out of which the SSCs formed.

6. Summary and Conclusions

In this paper we have presented new single dish and interferometric observations of the molecular gas and millimeter continuum of the starburst region in the dwarf galaxy Henize 2-10.

Our observations confirm earlier detections of the ^{13}CO and $\text{HCN}(1-0)$ line emission. The relatively strong detections of high density molecular tracers associated with the young Super Star Clusters confirm that this galaxy is undergoing vigorous star formation and is an ideal laboratory to study extragalactic starbursts.

In this context, our $\text{CO}(2-1)$ and 1.3mm continuum SMA observations, with a linear resolution of 60 – 80 pc, represent a first attempt to resolve the parent molecular clouds out of which SSCs may form. We reveal a rich population of molecular clouds with estimated masses and densities in the upper range of those measured in our Galaxy. The molecular gas accounts for approximately half of the total mass in the inner region of the galaxy, while the young stellar clusters account for the remaining mass.

We find possible evidence that the super star clusters are associated with very massive and dense molecular cores, but our observations and tracers do not allow us to confirm unambiguously their presence. New higher angular resolution and sensitivity observations of high density tracers and (sub-)millimeter continuum are required to clarify this possibility.

Acknowledgements. All the observations presented in this paper were performed by the observatories staff in service mode. We thank all the astronomers and operators on duty for delivering excellent observations and for delivering calibrated data packages very rapidly. In particular we thank Thomas Stanke and Carlos de Brueck for the Science Verification observations with APEX, Pierre Cox and Stephane Leon for the IRAM-30m DDT observations and Ray Blundell and Quzhou Zhang for scheduling additional SMA observations in the compact array. We also thank Kelsey Johnson and Jonathan Tan for providing the VLA 3.6cm map and for insightful discussions.

References

- André, P., Ward-Thompson, D., & Barsony, M. 2000, *Protostars and Planets IV*, 59
- Arimoto, N. and Sofue, Y. and Tsujimoto, T. 1996, *PASJ*, 48, 275
- Baas, F., Israel, F. P., & Koornneef, J. 1994, *A&A*, 284, 403
- Blitz, L., Fukui, Y., Kawamura, A., Leroy, A., Mizuno, N., & Rosolowsky, E. 2007, *Protostars and Planets V*, 81
- Braine, J., Combes, F., Casoli, F., Dupraz, C., Gerin, M., Klein, U., Wielebinski, R. & Brouillet, N. 1993, *A&AS*, 97, 887
- Brandner, W., Clark, J. S., Stolte, A., Waters, R., Negueruela, I. & Goodwin, S. P. 2008, *A&A*, 478, 137
- Cabanac, R. A., Vanzi, L. & Sauvage, M. 2005, *ApJ*, 631, 252
- Conti, P. S. & Vacca, W. D. 1994, *ApJ*, 423, 97
- Dowell, J. D., Buckalew, B. A., Tan, J. C. 2008, *AJ*, 135, 823
- Egan, M. P., Shipman, R. F., Price, S. D., Carey, S. J., Clark, F. O. & Cohen, M. 1998, *ApJ*, 494, 199
- Elmegreen, B.G. 2002, *ApJ*, 577, 206
- Galliano, F., Madden, S. C., Jones, A. P., Wilson, C. D. & Bernard, J.-P. 2005, *A&A*, 434, 867
- Güsten, R., Nyman, L. Å., Schilke, P., Menten, K., Cesarsky, C. & Booth, R. 2006, *A&A*, 454, 13
- Hillenbrand, L. A., & Hartmann, L. W. 1998, *ApJ*, 492, 540
- Ho, P. T. P., Moran, J. M. & Lo, K. Y. 2004, *ApJ*, 616, 1
- Imanishi, M., Nakanishi, K., Tamura, Y., Oi, N. & Kohno, K. 2007, *AJ*, 134, 2366
- Johnson, K.E., Leitherer, C., Vacca, W. D., & Conti, P. S. 2000, *AJ*, 120, 1273
- Johnson, K. E., & Koblunicky, H. A. 2003, *ApJ*, 597, 923
- Kennicutt, Jr., R. C. 1998, *ApJ*, 498, 541
- Koblunicky, H. A., Dickey, J. M., Sargent, A. I., Hogg, D. E., & Conti, P. S. 1995, *AJ*, 110, 116
- Koblunicky, H. A., & Johnson, K. E. 1999, *ApJ*, 527, 154
- Koblunicky, C. & Johnson, K. E. 2000, *astro.ph.*, 11409
- Lada, C. J. & Lada, E. A. 2003, *ARA&A*, 41, 57
- Launhardt, R. & Henning, T. 1997, *A&A*, 326, 329
- MacLaren, I., Richardson, K. M. & Wolfendale, A. W. 1988, *ApJ*, 333, 821
- Maloney, P. & Black, J. H. 1988, *ApJ*, 325, 389
- Marquart, T., Fathi, K., Å-Stlin, G., Bergvall, N., Cumming, R. J. & Amram, P. 2007, *A&A*, 474, 9
- Meier, D. S., Turner, J. L., Crosthwaite, L. P., & Beck, S. C. 2001, *AJ*, 121, 740
- Millar, T. J., Farquhar, P. R. A. & Willacy, K. 1997, *A&AS*, 121, 139
- Perault, M., Omont, A., Simon, G., Seguin, P., Ojha, D., Blommaert, J., Felli, M., Gilmore, G., Guglielmo, F., Habing, H., Price, S., Robin, A., de Batz, B., Cesarsky, C., Elbaz, D., Epchtein, N., Fouque, P., Guest, S., Levine, D., Pollock, A., Prusti, T., Siebenmorgen, R., Testi, L. & Tiphene, D. 1996, *A&A*, 315, 165
- Petitpas, G. R., & Wilson, C. D. 1998, *ApJ*, 496, 226
- Rohlfs, K., & Wilson, T. L. 1996, *Tools of Radio Astronomy*, XVI, 423 pp. 127 figs., 20 tabs.. Springer-Verlag Berlin Heidelberg New York. Also Astronomy and Astrophysics Library,

- Scoville, N. Z., Yun, Min Su, Sanders, D. B., Clemens, D. P., Waller, W. H. 1987, *ApJS*, 63, 821
- Solomon, P. M., Rivolo, A. R., Barrett, J. & Yahil, A., 1987, *ApJ*, 319, 730
- Strong, A. W., Bloemen, J. B. G. M., Dame, T. M., Grenier, I. A., Hermsen, W., Lebrun, F., Nyman, L.-A., Pollock, A. M. T. & Thaddeus, P. 1988, *A&A*, 207, 1
- Tan, J.C. 2008, in "Triggered Star Formation in a turbulent ISM", edited B.Elmegreen & J.Palous, IAU Symposium 237
- Tarchi, A., Neininger, N., Greve, A., Klein, U., Garrington, S.T., Muxlow, T.W.B., Pedlar, A. & Glendenning, B.E. 2000, *A&A*, 358, 95
- Vacca, W. D., & Conti, P. S. 1992, *ApJ*, 401, 543
- Vacca, W. D., Johnson, K. E., & Conti, P. S. 2002, *AJ*, 123, 772
- Vanzi, L., Combes, F., Rubio, M., & Kunth, D. 2009, *A&A*, 496, 677
- Verter, F. & Hodge, P. 1995, *ApJ*, 446, 616
- Whitmore, B.C. 2002, in: A Decade of Hubble Space Telescope Science, M. Livio, K. Noll, M. Stiavelli, Eds. (Cambridge Univ. Press, Cambridge, 2002), pp. 153-180.
- Williams, J. P., de Geus, E. J. & Blitz, L. 1994, *ApJ*, 428, 693
- Wilner, D. J., & Welch, W. J. 1994, *ApJ*, 427, 898
- Wilson, C. D. 1995, *ApJ*, 448, 97
- Wilson, C. D. & Scoville, N. 1990, *ApJ*, 363, 435
- Zylka, R. 1998, Pocket Cookbook for the MOPSI software